21 Atomic Force Microscopy: Interaction Forces Measured in Phospholipid Monolayers, Bilayers, and Cell Membranes

Zoya Leonenko · David Cramb · Matthias Amrein · Eric Finot

Abstract. Atomic force microscopy (AFM) is a powerful technique which is commonly used to image surfaces at the nanoscale and single-molecule level, as well as to investigate physical properties of the sample surface using a technique known as force spectroscopy. In this chapter, we review our recent research where we used AFM to investigate physical properties of phospholipid monolayers, bilayers, and cell membranes. We describe the experimental procedures for AFM imaging, force measurements, and theoretical models to analyze force spectroscopy data. The data obtained allowed correlations between AFM topography and local adhesion and mechanoelastic properties of supported lipid bilayers in water, supported pulmonary surfactant films in air, and the plasma membrane of epithelial type II cells. Finally, AFM was applied to help elucidate the effect of anesthetics and cholesterol present in the lipid films.

Key words: Phospholipid, Monolayer, Bilayer, Pulmonary surfactant, Bovine lipid extract surfactant, Epithelial type II cell, Atomic force microscopy, Adhesion, Cholesterol, Halothane

21.1
Introduction

Lipid membranes are integral components of the cellular organization in all living organisms [1]. As the major constituents of the biological membranes that form the outer boundary of cells and organelles they are involved in a vast number of biological processes. Their functions are to compartmentalize the cells, sort, regulate, and mediate biomolecular interactions. These complex functions are possible owing to the diverse physical-chemical properties of these membranes, which include two-dimensional fluidity, material elasticity, chemical diversity, and rich phase behavior [2]. Understanding the physical and chemical properties of lipid membranes [3, 4] and how they control biological processes is critical to our understanding of the molecular mechanisms of many diseases and finding a cure for them. The variety in structure and physical properties of cell membranes governs their biomolecular assembly and plays an important role in many fundamental biological processes [5]. For example, small, condensed rafts of spingolipids, cholesterol, and raft-associated protein play a crucial role in signaling, intracellular trafficking of lipids, platelet activation, membrane fusion, and protein binding [6, 7]. Lipid rafts present in a cell membrane serve as entry and exit sites for microbial pathogens, such as influenza virus, measles virus, and HIV. Lipid–protein mixtures not only form membranes. Pulmonary surfactant [8, 9], which is a specific lipid–protein complex,

forms a molecular film that covers the lung's interface with the air [10]. The major functions of pulmonary surfactant are to reduce the surface tension of the airspace–liquid interface, provide stability to the alveolar structure, and reduce the work of breathing [11]. Understanding the lateral distribution and interactions among the lipids and proteins in pulmonary surfactant monolayers is extremely important in order to develop methods of preventing alveolar collapse in cases of surfactant deficiency such as in premature infants or dysfunctional surfactant such as in adult respiratory distress syndrome (ARDS) [12].

Supported phospholipid bilayers (SPBs) [13] and monolayers are accepted and convenient model systems which mimic many fundamental properties of biological membranes and pulmonary surfactant. SPBs are composed of phospholipids adsorbed to a planar solid support. They also are of importance for biotechnology applications, as they form membrane-mimetic materials useful for creation of new classes of biosensors, diagnostic tools, and high-throughput characterization platforms for rapid and early detection of interactions between cells and their environment [14, 15]. Such lipid films can serve as templates into which functional biomolecules can be incorporated, creating a powerful platform for the development of nanosensor and nanodevices. For biomedical and nanotechnology applications it is important to control processes involving the interaction of lipid membranes and monolayers with DNA and proteins, as well as polymers and inorganic nanoparticles. Adhesion of particles to the supported lipid films is important in biotechnology and medicine applications, for example, to study toxicity of nanoscale air pollutants and also for the development of effective pulmonary drug delivery systems [16].

Atomic force microscopy (AFM) has proven to be a valuable tool for imaging "soft" biological samples such as lipid films [17–21] especially in intermittent contact mode [22–24]. With AFM, one can not only image membranes in their native hydrated state. One can also measure the forces of interaction between the AFM probe and the sample, obtaining information about the physical properties of biological systems [25–29].

Measuring the physical and chemical properties of lipid membranes and monolayers involves measuring a multitude forces of weak noncovalent bonds (e. g., electrostatic, van der Waals, and/or hydrogen bonds) or hydrophobic interactions between geometrically complementary surfaces. To understand a response of a biological system to its environment one needs to measure the physical and chemical properties of the macromolecular assembly, such as membranes and monolayers, and how these properties are affected by mechanical stress, thermal change, and/or molecular adsorption. It concerns the mechanical properties such as two-dimensional fluidity and anisotropic elasticity of the membrane as well as thermodynamic properties underlying its rich phase behavior. Those bulk properties can also be investigated by a thermodynamic approach such as calorimetry, densitometry, contact angle measurement, or analysis of adsorption kinetics using surface plasmon resonance or ellipsometry. On a molecular level, molecular dynamics simulation has been employed, providing an insight into the organization of lipid structures and the stability. AFM is an ideal tool to measure directly the molecular force from 0.1 pN up to micronewtons between two surfaces or even single molecules. On approach of the AFM probe tip to the sample, the force–distance curve can be used to characterize surface properties, such as van der Waals and electrostatic forces, solvation,

hydration, and compression-related steric forces [30]. The retraction force curves often show a hysteresis referred to as an adhesion "pull-off" event, which can be used to estimate the adhesion forces. Many experimental force data are now available in the literature, and theoretical models have been developed for the analysis of forces acting between two solid surfaces [31–36]. In contrast, only a few publications have addressed force measurements of soft thin layers [37] such as thiol self-assembled monolayers [38–41] and phospholipid bilayers [42–44].

Here we review our recent research on interaction forces measured with AFM on SPBs in water and supported phospolipid monolayers in air, as models for biological membrane and pulmonary lung surfactant films, and on epithelial type II cells which cover the lung's interface with the air.

21.2
Phase Transitions of Lipid Bilayers in Water

The complex structural dynamics of phospholipid bilayers are governed by temperature-dependent parameters such as average interfacial area per lipid, bilayer thickness, and disorder of the hydrophobic tails. Although SPBs differ from free-standing membranes such as those found in vesicles or liposomes, they serve as good models for biological membranes. The SPB can exist in several lamellar phases: gel phase, liquid-crystalline or fluid phase, subgel phase, and ripple phase [45]. Often, phase behavior is dominated by the main L_β–L_α (gel–fluid) transition. A large number of stable, metastable, and transient lamellar gel structures can be adopted by different lipids. For saturated phosphatidylcholines, such as 1,2-dipalmitoyl phosphatidylcholine (DPPC), there are four recognized lamellar phases, namely, a liquid-crystalline phase (L_α) or phases with ordered hydrocarbon chain arrangements, a ripple phase (P_β), a gel phase (L_β), and "subgel" or "crystal" phase (L_c) [46]. Phase-related bilayer properties have been examined using a variety of experimental techniques [47–50]. The phase transition from the gel phase to the liquid-crystalline phase is shown schematically in Fig. 21.1. Physical properties of lipids such as density and thickness have been studied by differential scanning calorimetry, pressure calorimetry or dilatometry, and densitometry and other methods [51, 52]. Temperature-dependent AFM studies allow for visualizing these phase transitions and provide valuable information about changes in structural and physical properties of bilayers during phase transitions. Temperature-dependent AFM studies involving imaging bilayers have been reported [53–57]. In addition, we have examined the force measurements as a function of temperature [58].

In this section we review our results on force measurements in SPBs during phase transitions associated with melting or anesthetic incorporation. Dioleoyl phosphatidylcholine (DOPC; lyophilized or in chloroform solution) (Sigma, Oakville, ON, USA) and DPPC (Avanti Polar Lipids, Alabaster, ME, USA) were used without further purification. Phosphate buffer (pH 6.8) and distilled, nanopure water were used in the preparation of all vesicles. Freshly cleaved ASTMV-2 quality, scratch-free ruby mica (Asheville-Schoonmaker Mica) was used as the solid support. Supported planar bilayers were prepared for AFM imaging by the method of vesicle fusion [59, 60]. All vesicles were prepared as previously reported [59]. Aliquots of

Fig. 21.1. Domain formation in a phospholipid bilayer supported on mica. The fluid phase domains correspond to a lower thickness than the gel-phase domains
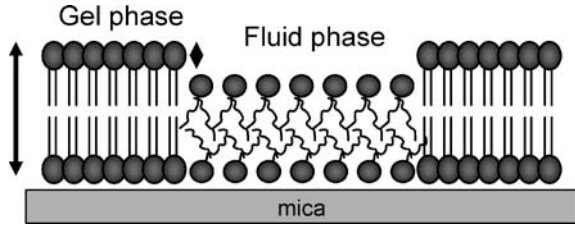
the vesicle solution were deposited on freshly cleaved pure mica. After a controlled period of time the mica was gently rinsed with nanopure water. Surfaces were imaged with an atomic force microscope (Pico SPM, Molecular Imaging) equipped with an AFMS-165 scanner. The nominal spring constants of Au–Cr-coated MAClevers used were approximately 0.6 N/m. The tip radius of curvature was typically 25 nm. The scan rate was 20 μm/s. All imaging and force measurements were performed in a liquid cell under nanopure water. For temperature-dependence experiments the temperature was varied from 22 to 65 °C, within 0.1 °C accuracy with a 1 °C/min ramp.

21.2.1
Morphology Change During Lamellar Phase Transition

21.2.1.1
Temperature-Dependent Phase Transition

A DPPC phospholipid bilayer normally exists in the gel phase at room temperature. When heated above the melting transition temperature it transforms into the fluid phase. Domains of lower thickness are readily formed during this process. Such domains are shown schematically in Fig. 21.1 and are easily observed by AFM imaging (Fig. 21.2).

A DPPC supported bilayer was imaged while it was heated from room temperature to 65 °C and also while it was cooled back to room temperature. The topography images (Fig. 21.2) show the typical formation of lipid domains during the phase transition. In Fig. 21.2, panel A, a DPPC bilayer is in the gel phase, L_β, at 22 °C. When sample was heated, several phase transitions were observed as a function of increasing temperature: a broad main transition was observed at 42–52 °C, and another transition at 53–60 °C within the fluid phase. The first transition, at 42–52 °C, is attributed to the main L_β–L_α transition, and the second transition, between 53–60 °C, to the formation of a fluid disordered phase, perhaps with interdigitated or partly interdigitated lipid chains. Slowly cooling the system back showed that the two higher-temperature transitions at 42–52 and 53–60 °C are reversible and that the bilayer can be restored to its initial thickness [61]. A DOPC bilayer, which exists in a fluid phase at room temperature, when heated shows thickness reduction as well as an increase in surface coverage [62], but no domain formation. Previous studies have established the L_β–L_α phase transition temperature for DPPC at 41 °C [63]. The presence of two broad transitions that we observed on supported bilayers can be attributed to the effect of the mica support and to separating the phase transitions
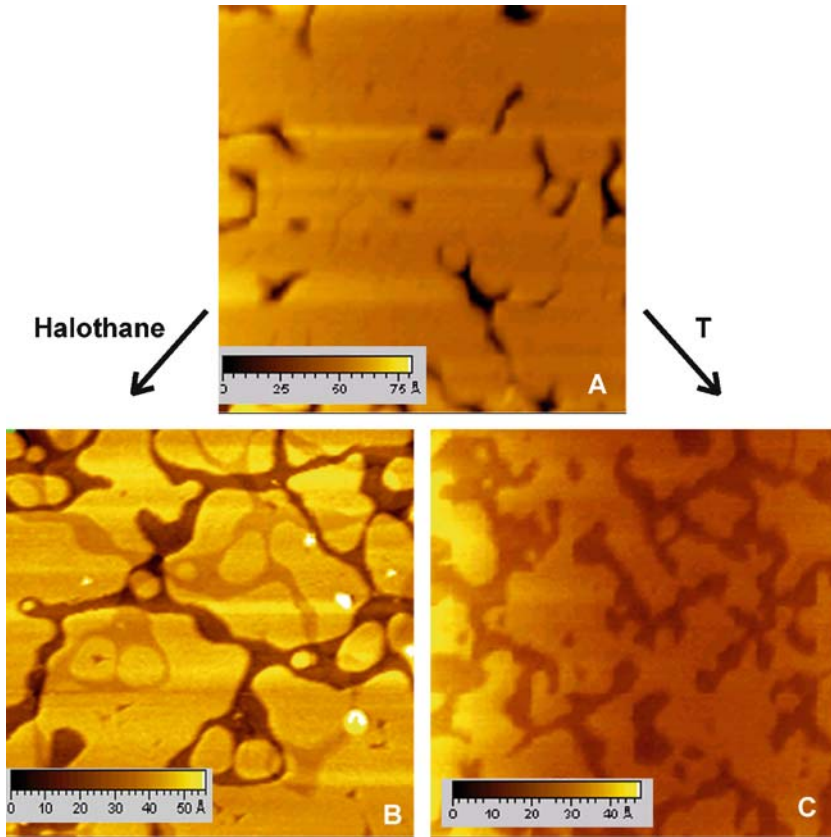
Fig. 21.2. Atomic force microscopy (AFM) topography images (scan size 1.5 μm by 1.5 μm) showing a phase transition in a 1,2-dipalmitoyl phosphatidylcholine (DPPC) bilayer. **A** DPPC bilayer at room temperature, 22 °C. **B** DPPC bilayer with excess of halothane (60 μl) [57]. **C** 50 °C—melting transition [61]. The *scale bars* show the deviation in height

in the bilayer's upper and lower leaflets. A similar effect was reported for supported bilayer transitions observed using differential scanning calorimetry by Yang and Appleyard [64].

21.2.1.2
Phase Transition Due to Incorporation of Halothane

Understanding the changes in physical and chemical properties of biological membranes owing to the incorporation of anesthetics is of great interest for understanding the mechanism of anesthetic action. Currently, it is understood that anesthetic directly affects membrane proteins; however, because they are lipophilic, they partition into the membrane and may interact with membrane proteins via the lipid bilayer.

AFM imaging of a DPPC bilayer (Fig. 21.2, panel B) shows domain formation in the presence of general anesthetic halothane similar to what we observed during

heating. We have shown that changes in bilayer thickness induced by halothane are similar to the first melting transition [58]. For a DPPC SPB containing halothane, only one transition at 52–60 °C was evident during heating and cooling. The presence of halothane changes the structural properties of the bilayer in such a way that the other transitions observed for the pure bilayer are not possible. We assume that in the presence of halothane, the water interface layer is disturbed by halothane molecules, thus eliminating the low-temperature transition. In spite of the visual similarity between an anesthetic-induced domain formation (Fig. 21.2, panel B) and the heat-induced gel–liquid phase transition (Fig. 21.2, panel C), observed by AFM imaging, the mechanism of anesthetic action is likely to be different from the effect of membrane melting. We assume that the physical properties of the domains produced in lipid bilayers by halothane and by temperature are also different. To address these physical properties we used the atomic force microscope also as a force apparatus.

21.2.2
Change in Forces During Phase Transition

21.2.2.1
Force Measurements

In AFM force measurements, the probe is moved towards the sample and cantilever deflection is measured as a function of the extension of the piezoelectric tube. During approach to the surface, the attractive and repulsive forces measured are characterized by van der Waals and electrostatic interactions as well as solvation, hydration, and compression-related steric forces [26, 36, 52, 65]. The probe is then retracted from the surface. The retraction force curves often show a hysteresis referred to as an adhesion pull-off event, which can be used to determine adhesion forces between the probe and the sample.

In our experiments, we imaged the supported bilayer first in tapping MAC mode. After the image was complete and had been saved we switched the regime into the contact mode and then using the same cantilever, we measured forces of interaction by positioning the atomic force microscope tip on different locations using the image obtained in tapping mode.

It is a well-known fact that the force interactions depend on the velocity of the surface approach [26], especially for soft, viscoelastic materials. We varied the frequency sweep over about four decades, from 0.01 to 10 Hz. The Z-range was 50 nm. Note that varying the scan frequency affects simultaneously the velocity at which the tip is withdrawn from the bilayer and the contact time between the tip and the sample. At a fixed applied load, increasing the frequency sweep rate increases the tip velocity, but decreases the contact time. Data were collected over a time period of 2 h at ten locations on the bilayer and a total of 100 force curves were analyzed for each sample. Force curves were saved as plots and then converted into text files for analysis. After the raw data had been collected they were converted into the "force versus separation plots", averaged, and analyzed.

Here we review our results on force measurements in DOPC and DPPC SPBs during heating above T_M from 22 to 65 °C. We also compare them with results obtained on bilayers saturated with halothane at 20 °C.

21.2.2.2
AFM Force Analysis

Force measurements using the atomic force microscope (described in Sect. 21.2.2.1) give us raw data of cantilever deflection δV versus piezo movement z_{piezo}. Raw data were transformed numerically using the MatLab environment. Raw data (Z_c versus Z_p) were then converted into force F versus surface–tip separation D using Hooke's law: $F = kZ_c$, where k is the spring constant of the cantilever, and the geometric relationship $D = Z_c - Z_p$ for incremental changes.

Statistical data were extracted from a large set of measurements. The bin size of the histogram was determined statistically by dividing the range of measurements by the square root of the number of measurements. The average of the adhesion force and the standard deviation were obtained from the analysis of the whole set of force curves, which were represented in histogram form, $P(x)$, and then adjusted using Gaussian and Poisson distributions.

21.2.2.3
Adhesion Forces

To extract information about adhesion forces we analyzed the retrace part of the force curve. Raw data of the cantilever deflection corresponding to the retraction of the tip from the surface, after contact, are shown in Fig. 21.3.

Force data were collected as a function of temperature for a DPPC SPB. When a pure DPPC bilayer was heated, the temperature increase resulted in a gradual change of the force profile. The force required to detach the tip from the bilayer increased from 3 nN at 36 °C to 10 nN at 50 °C. In addition, the jump out of the contact was not abrupt, compared with that for a "solid-like" surface (i. e., mica). The distance the tip travels before it separates from the surface increased with increasing temperature. As van der Waals forces are known to vary only slightly with temperature, the change in the profile must be due to tip–bilayer interactions that depend on the bilayer phase. Incorporation of halothane into DPPC also leads
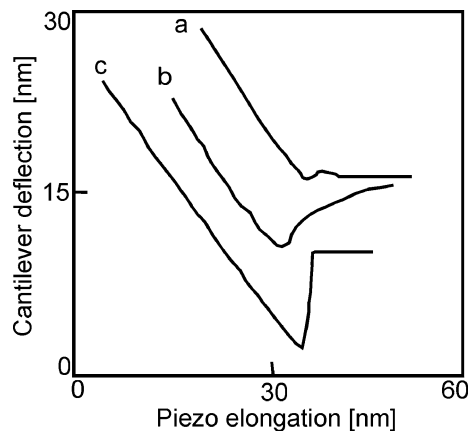

Fig. 21.3. Cantilever deflection dZ_c as a function of the piezotube elongation when the tip is retracted from the sample. DPPC bilayers deposited on mica were measured under three conditions: **a** the DPPC bilayer at 22 °C; **b** the DPPC bilayer at 50 °C; **c** the DPPC bilayer with halothane incorporated at 22 °C

to a significant change in the force profile. As a bilayer adsorbed on mica is known to screen the van der Waals forces [66], the huge adhesion force observed cannot originate solely from the van der Waals forces. This adhesion behavior can be compared with that observed in the phase transition on DPPC from the gel to the liquid crystal observed on increasing the temperature (Fig. 21.3, plots b and c). Halothane induces then a transition of the bilayer into the fluid phase in a similar manner as melting, and induces the increase in adhesion, although the adhesion with excess halothane was greater than the adhesion observed on pure DPPC at elevated temperature.

To analyze the force histogram (Fig. 21.4), we employed Poisson statistics. It has been demonstrated that the force of a unit interaction between an atomic force microscope tip and a surface can be determined from a statistical analysis of a series of detachment force measurements. For a statistical analysis based on adhesion force originating from a discrete number n of individual interactions or bonds, F_s was used. The total force distribution follows Poisson statistics, where both the adhesion force F_{adh} and the variance σ originate from a number of individual tip–surface bonds, n:

$$F_{adh} = n F_s \quad \text{and} \quad \sigma^2 = n F_s^2 . \tag{21.1}$$

The force of one bond, F_s, is therefore given by the square of the variance of the force divided by the mean adhesion force F_{adh}. The value n is the ratio between F_{adh} and F_s. This analysis has the advantage that knowledge of the mean radius of curvature is not required [67] and gives information on the nature of the bilayer. This analysis allows one to correlate microscale changes in the bilayer physical properties with
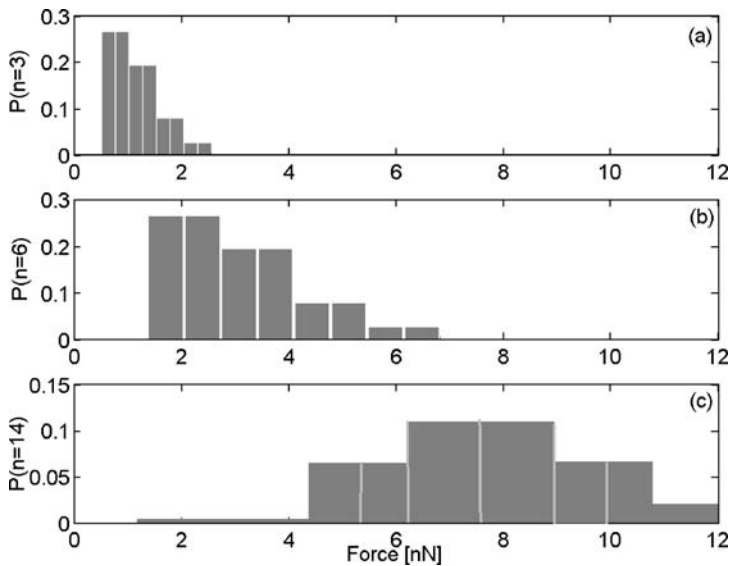
Fig. 21.4. Distribution of adhesion force F_{adh}, measured in phospholipid bilayers in water: **a** DPPC $F_s = 0.3$ nN, $n = 3$; **b** DPPC $F_s = 0.5$ nN, $n = 6$ [58]; **c** DPPC + halothane $F_s = 0.5$ nN, $n = 14$ [58]

Table 21.1. Experimental adhesion force F_{adh} and its standard error σ on a 1,2-dipalmitoyl phosphatidylcholine (DPPC) bilayer at room and elevated temperature and DPPC with halothane, measured at room temperature; calculation of the number of bonds n and the mean force of a single bond F_s

	DPPC[a] 22 °C	DPPC[b] 22 °C	DOPC[a] 22 °C	DPPC[a] 60 °C	DPPC + halothane[b] 22 °C
F_{adh} (nN)	1	1.5	3	5	7
σ (nN)	0.6	0.8	1.2	2	2
F_s (nN)	0.3	0.4	0.5	0.8	0.5
n	3	4	6	6	14

DOPC dioleoyl phosphatidylcholine
[a] From [61]
[b] From [58]

the molecular structure and the mobility of individual lipid molecules. The lipids in biological membranes have a high lateral mobility since they can easily exchange their positions. The fluidity of the membrane can be then thought of as the lateral motion of the constituents of the membranes. This fluidity should depend on the chain length and the composition of the membranes. The mobility of tails can be seen as the number of molecules n in contact with the AFM probe. The larger n is, the higher the mobility. The change in mobility increases the number of bonds n and therefore F_{adh} and σ.

The statistical distribution of the adhesion forces (Table 21.1) clearly demonstrates that adhesion forces observed for a pure DPPC bilayer increase with heating and increase even more with halothane incorporation.

A fluid-phase DPPC bilayer at high temperature is typically ascribed to a higher number of tip–sample bonds [61]. The force of a single bond is increased in a fluid phase. In addition, in a fluid phase, n increases on decreasing the speed of the tip motion v. The number of bonds, n, involved is higher in the fluid phase. It has been shown previously that the force required to remove a single lipid from a bilayer is of the order 30–140 pN [68,69], depending on the lipid and on the technique employed. The lowest values that we measure are at least twice this range, suggesting that we do not observe single lipid binding events. Instead, our unit "bonds" must represent patches containing more than three lipids. The detachment force between the patch and the tip must be smaller than the extraction force of the entire patch otherwise we would see evidence of lipids coating the tip. This is consistent with our previous work where continuous imaging of bilayers displayed no resolution degradation or changes in force curves, which would result from uncontrollable lipid coating the atomic force microscope tip.

The effect of halothane is similar to the effect of melting. A DPPC bilayer with halothane corresponds to higher adhesion force, higher standard error, and a larger number of single binding events between the atomic force microscope tip and the sample. This number, $n = 14$, is more than 2 times larger than for a fluid phase produced by melting. The single force F_s was not altered significantly by the presence of halothane. The presence of halothane in the bilayer increases,

therefore, the fluidity of the DPPC molecules in the bilayer. The number of binding events, n, could also be higher owing to the contribution of halothane molecules themselves, interacting with the atomic force microscope tip. The unit force F_s for fluid-phase DPPC is 0.8 compared with 0.5 for the DOPC bilayer (Table 21.1); the umber of unit bonds is 6 for both fluid-phase DPPC and DOPC bilayers. This correlation permits evaluation of a bilayer fluidity and is in a good agreement with imaging data. Adhesion forces depend, therefore, on the physical properties of the bilayer and the force analysis gives valuable information on the nature of the bilayer.

21.2.2.4
Repulsive Forces

Repulsive forces were extracted by analyzing the approach part of experimental force curves. Figure 21.5 shows plots of the repulsive forces measured while the atomic force microscope tip was approaching the sample surface of pure mica for a DPPC bilayer at room temperature, a DPPC bilayer at 50 °C [61], and a DPPC bilayer with an excess of halothane [58].

For pure DPPC, three exponential regimes clearly exist, one at the long range from 4 to 7 nm, another at short range between 0.3 and 4 nm, and the third, steep one in close contact with mica, which we will not consider.

The *long-range* interactions can be explained by *electrostatics*. Electrostatic repulsion likely originates from an effective charge density at the bilayer–water interface, where zwitterionic headgroups interact with water molecules. The approximate expression of the electrostatic force (also called double-layer force) is given by [70]

$$F = 4\pi\sigma R\psi_T \exp(-K_D D) , \qquad (21.2)$$

where R is the tip radius, σ is the surface charge, ψ_T is the tip potential, and K_D is the inverse of the Debye length. K_D can be estimated to be 0.25/nm.
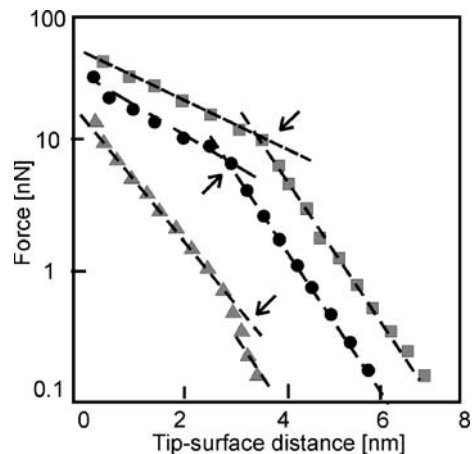
Fig. 21.5. Logarithmic representation of the force acting on the DPPC layer at 22 °C (*squares*), on the DPPC layer at 50 °C (*circles*), and on the DPPC layer with halothane at 22 °C (*triangles*)

The long-range force does not seem to be affected by temperature, as the two curves in the log plot are almost parallel (Fig. 21.5). In the presence of halothane, (Fig. 21.5), the long-range electrostatic forces appear to be reduced, in the range above 4 nm. Therefore, halothane clearly changes the surface charge density of the DPPC bilayer by replacing water molecules and reducing water shielding of the lipid bilayer, thereby decreasing the magnitude of the electrostatic forces.

The second, *short-range* regime, between 0.3 and 4 nm, is attributed to the *deformation of the bilayer*. Most studies on the bilayer report a jump corresponding to the piercing of the bilayer for forces ranging from approximately 3 to 25 nN [71–73]. This jump into contact is observed when the force gradient exceeds the spring constant of the cantilever k, which is the case when $k < 1$ N/m. Although the force sensitivity can be altered, a high cantilever spring constant ($k = 30$ N/m) was chosen for monitoring all the data during the penetration. The force gradient attributed to the layer indentation was measured to be around 10 N/m and the force needed to puncture the lipid bilayer is in good agreement with that found in other studies.

The repulsive force in the short-range regime at the contact of the bilayer cannot be easily treated using common elastic mechanical models such as Hertz's theory, or any other models based on continuum mechanics. The heads of the phospholipids are responsible for a crystalline elasticity, i.e., a change of the head-to-head distance (high elasticity but low rupture). The lipid chain behaves like rubber (low elasticity), and this behavior is related to the change of entropy (increase of order when one presses the layer). It results in the property that the cell membranes can be easily deformed in the plane but do not resist the expansion (distance between the headgroup cannot vary more than 2%). With our AFM experiments we are examining very small, discrete areas where nanoindentation induces not only macroscopic compression of the bilayer, but also nanoscale structural changes in the bilayer. Therefore, a molecular approach, considering steric forces [42], is preferable.

The exponential increase of the repulsive force likely originates from tail steric repulsion induced by the atomic force microscope tip compressing the bilayer. The tails in the bilayer will resist compression, because compression will increase the local concentration of the alkyl segments, increasing the free energy of the system. The steric forces of compression act on the bilayer until the loading force is close to the yield force, when the tip penetrates through the bilayer. The breakthrough force decreases as the temperature increases, and a DPPC bilayer at elevated temperatures shows similar instability in the force plot as a fluid-phase DOPC bilayer and a fluid-phase 1,2-dioleoyl-3-trimethylammonium propane (DOTAP) bilayer [44].

The steric force per unit area that the bilayer exerts on the tip can be modeled using the formalism developed in the work of de Gennes [74]. This model was further developed by Cappella and Dietler [26], where interaction between two polymer surfaces was considered. We modified this formula, considering the interaction of the AFM probe and the bilayer, which gives the formula for the steric repulsion force:

$$F_{\text{ste}} = 100kTRL\gamma^{3/2} \exp(-2\pi D/L) , \qquad (21.3)$$

where k is the Boltzmann constant, R is the tip radius of curvature, T is the temperature, γ is the tail density (inverse of the area per lipid), D is the distance between

the atomic force microscope tip and the mica surface, and L is the uncompressed bilayer thickness. Similar to the equation for the two interacting polymer surfaces, this formula is valid in the range of distances where $0.2 < D/L < 0.9$. Since the tip radius is not well defined, it is difficult to estimate the tail density from the fit, but the transition between the two exponential regimes can be a good way to measure the thickness of the bilayer L.

The steric forces can, however, be used to determine the thickness of the layer adsorbed at the surface in good agreement with the image cross-section analysis. With the temperature increase, the steric force departs from a pure exponential law owing to the increase of the lateral mobility of the phospholipid tails. The transition between the electrostatic regime and the steric regime where the tip is at the top of the bilayer can be an effective way to estimate the bilayer thickness. At 22 °C, a transition occurs at $D = 4$ nm, corresponding to a thickness $L = D/0.9 = 4.5$ nm, which agrees with what is known from the literature (4.7 nm). With increasing temperature, the magnitude and the range of the steric force decrease contrary to the change in the electrostatic force. The steric force in a fluid phase, at elevated temperatures, is reduced by 50% compared with that a gel phase, as in Fig. 21.5. This can be explained by the reduction in the tail density with temperature. The tail density is reduced from $1/50$ to $1/67.1$ (considering an area per lipid of $50\,\text{Å}^2$ at room temperature and $67.1\,\text{Å}^2$ at 65 °C [75–77]), which makes 25% of difference and therefore a change of 40% in the force. In a fluid regime, i.e., at $T > 50$ °C, the shape of the steric part of the force–distance curve starts to depart from an exponential dependence and is similar to the linear abrupt jump observed for a fluid-phase DOTAP bilayer at room temperature. It appears that (21.3) is only valid for a gel-phase DPPC bilayer, where lateral motion of the lipids is lower.

With halothane incorporation (Fig. 21.5, triangles) the force is mostly governed by the bilayer deformation, described by steric forces. The induced phase transition of the DPPC has already been characterized by a decrease in the "effective thickness". The major difference with the temperature-induced phase transition comes from the fact that the incorporation of halothane changes the electrostatic interaction, which was not the case during the melting transition. Our force measurements confirmed that assumption and clearly showed the differences in the physical properties of the bilayer in thin domains, produced by the melting transition and partitioning of halothane.

When the adhesion forces are compared for DPPC and DOPC bilayers, they are similar for the fluid-phase DPPC bilayer at elevated temperatures and the fluid-phase DOPC bilayer at room temperature. The unit force F_s for fluid-phase the DPPC bilayer is 0.8 compared with 0.5 for the DOPC bilayer (Table 21.1); the number of unit bonds is 6 for both fluid-phase DPPC and DOPC bilayers. This correlation permits evaluation of a bilayer fluidity and is in a good agreement with imaging data. Therefore, adhesion forces depend on the physical properties of the bilayer, and force analysis gives important information on the nature of the bilayer. In the repulsive part of the force plot using a steric force model also provides an important insight into the properties of the bilayer and ability of lipids to resist compression. Steric forces reduce with the temperature increase for the DPPC bilayer and correlate well with low steric forces for the fluid-phase DOPC bilayer at room temperature. In general, a fluid-phase bilayer can be characterized by the reduced

repulsive forces, compared with the gel-phase bilayer. The major contribution to this change is provided by changes in steric forces. Lipid compression is much easier in the fluid phase owing to the higher disorder of tails and mobility of lipids, and lower tail density.

Individual bond forces can be estimated for lipid bilayers and changes in binding number can be used as a distinctive feature of the increase of bilayer fluidity. A force analysis revealed that the interaction between the tip and the surface was governed by both the electrostatic forces, for longer range, and the steric forces, at shorter range. Electrostatic repulsion likely originates from an effective charge density at the bilayer–water interface, where zwitterionic headgroups interact with water molecules. The steric forces can be used to determine the thickness of the layer adsorbed at the surface in good agreement with the image cross-section analysis. With the temperature increase, the steric force departs from a pure exponential law owing to the increase of the lateral mobility of the phospholipid tails. The transition between the electrostatic regime and the steric regime where the tip is at the top of the bilayer can be an effective way to estimate the bilayer thickness.

The temperature-induced phase transition of DPPC has been characterized by a decrease in the, "effective thickness" and we also observed similar behavior for bilayers containing halothane [58]. The major difference comes from the fact that the incorporation of halothane changes the electrostatic interaction, which was not the case during the melting transition. Halothane is a small polar molecule and is assumed to increase the polarity of the bilayer at the interface, and has been shown to replace water molecules bound to lipids at the interface. Our force measurements confirmed that assumption and clearly showed the differences in the physical properties of the bilayer in thin domains, produced by the melting transition and partitioning of halothane.

21.3
Force Measurements on Pulmonary Surfactant Monolayers in Air

Pulmonary surfactant is a specific mixture of phospholipids and surfactant-specific proteins. It forms a molecular film at the interface of the hydrated lung epithelium with the air and thereby reduces the surface tension of the interface to near zero. This is required for normal respiration and structural stability of the lung. In adult respiratory distress syndrome (ARDS), surfactant function fails. As a result, the lung is less compliant, the gas exchange area is reduced, and blood oxygenation is strongly decreased. The surfactant film is also the first barrier of airborne particles in polluted air. When inhaled, ultrafine particles with an aerodynamic diameter of 100 nm or less produce a major health threat. They cross the surfactant film, cross the lung epithelium, and enter the bloodstream. We describe force spectroscopy experiments aimed at a better understanding of surfactant failure in ARDS. Force spectroscopy was used to study the interactions between airborne particles and the surfactant. Particles (modeled by an atomic force microscope tip) interact with the surfactant film before they get into close contact because of the electrical surface potential of the film. This interaction depends on surface potential, which is locally strongly variable, depending on the film composition.

Fig. 21.6. Supported lipid mono-
layer and multilayers on mica, trans-
ferred from the liquid–air interface by
Langmuir–Blodgett deposition; these
multilayers are shown on the AFM
topography image in Fig. 21.7a
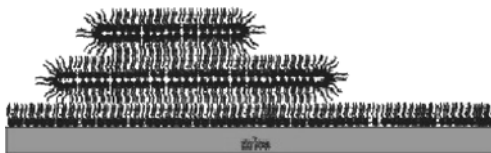
We have shown that the ability of surfactant to reduce surface tension is as-
sociated with a distinct molecular architecture of the surfactant film. The func-
tional pulmonary surfactant forms a pattern of molecular monolayer areas and ar-
eas of lamellar stacks, cross-linked to the monolayer at the air–aqueous interface
(Fig. 21.7a). We recently found that cholesterol in excess of a physiological propor-
tion abolishes surfactant function, and surfactant fails to lower the surface tension
upon compression [78]. This failure of function is associated with a change in the
molecular architecture [79]. The formation of multilayer stacks, which is a char-
acteristic feature of functional surfactant, does not occur in the presence of excess
cholesterol.

We performed atomic force measurements on supported pulmonary surfactant
films in air to address the effect of cholesterol on the physical properties of lung
surfactant films. We used bovine lipid extract surfactant (BLES). BLES is a hy-
drophobic extract of bovine lung lavage that differs from natural surfactant in the
lack of surfactant-specific proteins SP-A and SP–D and cholesterol. Phosphatidyl-
cholines represent 80% of its mass with half of the phosphatidylcholines being
the disaturated DPPC. Between 5 and 10 mass % is the negatively charged phos-
phatidylglycerol, and two hydrophobic surfactant-associated proteins (SP-B, SP-C).
BLES in nonbuffered normal saline (pH 5–6) with a phospholipid concentration
of 27 mg/ml was a kind gift from the manufacturer (BLES Biochemical, Lon-
don, ON, Canada). Cholesterol was purchased from Sigma Chemicals. A solu-
tion of 1:1:1 methanol, chloroform, and BLES by volume was first vortexed and
then spun at $100g$ for 5 min. The methanol–water phase was discarded and the
BLES in chloroform was retained and either 5 or 20% of cholesterol (by mass)
with respect to phospholipids in chloroform was added. Each solution was then
dried under N_2 and resuspended with Goerke's buffer [140 mM NaCl, 10 mM N-(2-
hydroxyethyl)piperazine-N'-ethanesulfonic acid and 2.5 mM $CaCl_2$; pH 6.9] to ob-
tain an aqueous suspension of BLES and cholesterol at a concentration of 27 mg/ml
phospholipids. BLES solutions were spread at the air–liquid interface. Supported
planar monolayers on mica were prepared using Langmuir–Blodgett technique and
transferred on mica support when films were compressed to a surface tension of
25 mN/m. Supported films were imaged in air using a NanoWizard atomic force
microscope from JPK Instruments, Germany. All measurements were performed
at 25 °C, over five different velocities, collecting each time ten force curves. Sil-
icon cantilevers from Micromash, Spain, were used with cantilever spring con-
stants of 0.6 and 0.7 N/m as determined by a thermofluctuation method using JPK
SPM software. Forces were measured on several different structural areas of the
film, by positioning the atomic force microscope tip after the image had been col-
lected.

21.3.1
Adhesion Measurements: Monolayer Stiffness and Function

Atomic force measurements helped us to elucidate how the loss of mechanical stability is related to the local mechanical properties of the film. Films containing 5 and 20% w/w cholesterol were compared. The presence of 20% cholesterol in BLES resulted in a decrease of the observed adhesive interaction, and an increase in the rigidity of the film. The force measurements were performed both on the monolayer area and on a first bilayer adjacent to the monolayer. The typical height of the bilayer area is 4.5 nm, and that of the monolayer is 2.5 nm. Typical areas where forces were measured are shown in Fig. 21.7a. For BLES with 20% cholesterol, only a monolayer was present and was used for force measurements (Fig. 21.7a, point 1).

BLES with 5% cholesterol at the bilayer area has an adhesion of 60 nN, which is higher than that of the monolayer. BLES with 20% cholesterol has a lower adhesion than the BLES monolayer with 5% cholesterol. It is interesting that the "single force" F_s was slightly lower in the presence of 20% cholesterol, 3 nN compared with 4 nN with 5% cholesterol, but the number of bonds decreased significantly from 15 and 10 to 7 (Table 21.1 [79]). Therefore, the presence of 20% cholesterol decreases the fluidity of the monolayer.

A force histogram (Fig. 21.8) was used to estimate the single force F_s and the number of bonds n. It is interesting that F_s was slightly lower in the presence of 20% cholesterol, 3 nN compared with 4 nN with 5% cholesterol, but n decreased significantly from 15 and 10 to 7 (Table 21.2). Therefore, the presence of 20%cholesterol decreases the fluidity of the monolayer.


A   B
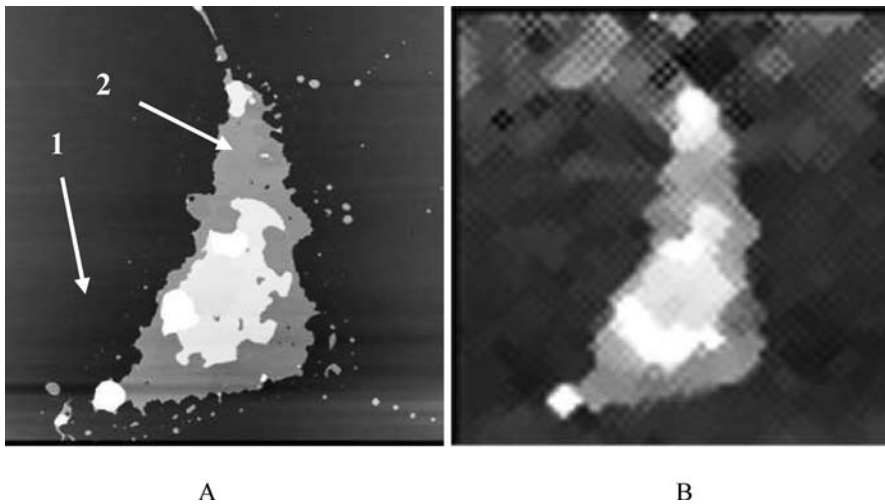
Fig. 21.7. A AFM topography image of supported bovine lipid extract surfactant (BLES) film, scan area 15 µm by 15 µm. **B** Adhesion force map image 64 by 64, collected on the same area. The adhesion force map was collected while forces of interaction at each of 64 by 64 points were measured. The adhesion peak of the retrace plot was used to generate the adhesion force map image. *1* area of a typical monolayer; *2* area of a typical bilayer, adjacent to a monolayer

Table 21.2. Experimental adhesion force F_{adh} and its standard error σ on a bovine lipid extract surfactant (*BLES*) bilayer with with 5% cholesterol, a BLES monolayer with 5% cholesterol, and a BLES monolayer with 20% cholesterol, measured at room temperature; calculation of the number of bonds n and the mean force of a single bond F_s. Rate 200 nm/s, load 20 nN. Adhesion force on pure mica does not exceed 1.5 nN

	BLES 20% cholesterol monolayer	BLES 5% cholesterol monolayer	BLES 5% cholesterol bilayer
F_{adh} (nN)	20	40	60
σ (nN)	8	12	15
F_s (nN)	3	4	4
n	7	10	15

Fig. 21.8. Distribution of adhesion force, F_{adh}, in air: **a** BLES monolayer + 20% cholesterol; **b** BLES monolayer + 5% cholesterol; **c** BLES bilayer + 5% cholesterol
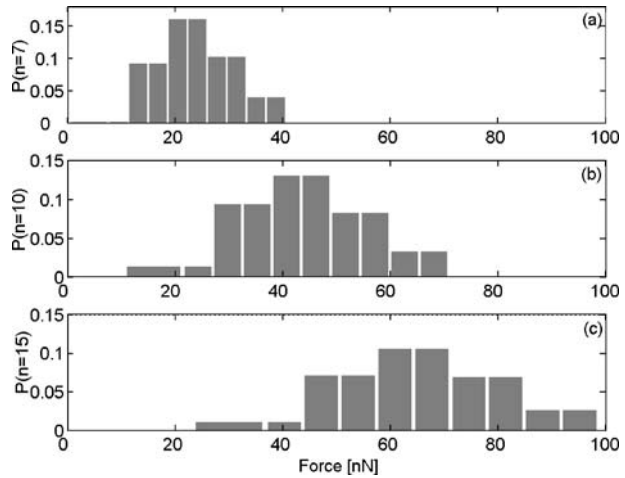
The increase in the adhesion force for a bilayer as compared with a monolayer may be understood by an increase in the contact area between the AFM probe and the sample at a given load. BLES with 20% cholesterol shows the lowest adhesion force, compared with monolayer and multilayer areas of BLES with 5% cholesterol. This indicates that adhesion properties of the film were considerably altered by the incorporation of 20% cholesterol, decreasing adhesive interaction, and increasing the rigidity of the film. The lipid molecules are not mobile enough in the presence of 20% cholesterol and cannot be easily rearranged around the tip to increase the contact area and adhesion force. The increased rigidity of the film and decreased adhesion that we observed may play an important role in preventing the monolayer–bilayer conversion.

21.3.2
Repulsive Forces: The Interaction of Charged Airborne Particles with Surfactant

The repulsive forces (Fig. 21.9) observed in air between the lipids film and the AFM probe were analyzed using two theoretical models for electrostatic interaction. The atomic force microscope tip was modeled once as a point charge and once as

Fig. 21.9. Electrostatic force measured in air on BLES film with 0% cholesterol (*top*) and with 20% cholesterol (*bottom*). Experimental data are shown by *dots* and theoretical fits with the point-charge model are drawn in *solid lines*
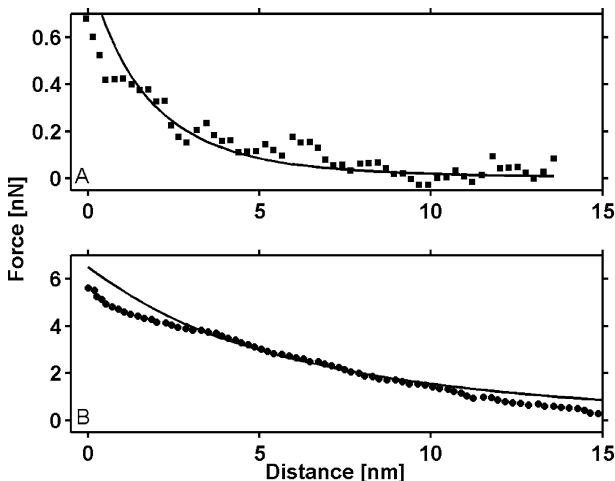
a charged semisphere. Here q is a charge of the atomic force microscope tip, k is a constant, ε is the dielectric permittivity of the medium, and r is the separation distance between the tip and the medium. The supported BLES surfactant monolayer is composed of lipid molecules, which are organized and oriented in such a way that the dipole moment is directed along the surface normal. Therefore, the patch of the monolayer can be treated as two charged planes, each having charge Q_+ and Q_- and surface charge density σ_+ and σ_-, with the separation distance δ_o, which corresponds to the thickness of the monolayer and is equal to 2.5 nm. The surface charge density of the sample, σ, is related to the surface potential V, which we have determined experimentally using Kelvin probe force microscopy [80, 81] and used here as a parameter.

In the case of a point charge, the total electrostatic force acting on q is given by

$$F = \frac{V_q}{2\delta_0 A_0} \left(\frac{\beta}{\sqrt{1+\beta^2}} - \frac{\alpha}{\sqrt{1+\alpha^2}} \right) , \qquad (21.4)$$

where

$$\frac{D}{R_0} = \alpha ,$$
$$\frac{D + \delta_0}{R_0} = \beta .$$

For the semisphere model, the force acting on the semisphere tip with a radius R_{so} will be

$$F_s = \frac{V_q}{2\delta_0 A_0} \left(\sqrt{1+\beta_1^2} - \sqrt{1+\alpha_1^2} - \sqrt{1+(\beta_1 - \gamma)^2} + \sqrt{1+(\alpha_1 - \gamma)^2} \right) ,$$
$$(21.5)$$

where

$$\frac{D + R_{S0}}{R_0} = \alpha_1 \, ,$$

$$\frac{D + R_{S0} + \delta_0}{R_0} = \beta_1 \, ,$$

$$\frac{R_{S0}}{R_0} = \gamma \, .$$

Kelvin probe microscopy was used [81] to determine the surface potential of the lipid layer in air. Cholesterol induces a nonuniform distribution of the electric surface potential even at small physiological concentrations, showing nanoscale domains in the Kelvin image, while the AFM topography image remains uniform. Such domains vary in surface potential from -0.6 V, measured for 0% cholesterol, to -0.4 V, at 20% cholesterol.

Both models we used fit the experimental data well, showing the presence of electrostatic interactions in the net force measured between the tip and the sample. To better fit the experimental data we varied the charge on the atomic force microscope tip and the size of the charged disks, R_0, which experimentally corresponds to the size of domains already observed with both AFM and Kelvin probe force microscopy imaging. We modeled the AFM probe also with a charged sphere; in this model the effective charge depends on the radius of the tip. Samples of BLES with 20% cholesterol exhibit stronger electrostatic repulsion at longer distances, for all models used.

Interestingly, the electrostatic force was found to be more sensitive to the size of these domains than to the changes in the surface potential observed owing to the effect of cholesterol. The experimental data and the theoretical fit correlate well and both revealed that the size of the domains is approximately 5 times larger for the film containing 20% cholesterol than that for the film with no cholesterol present. This confirms the important role of cholesterol—it produced small domains which differ by electrostatic potential, initially invisible with AFM, which causes the increase in the total electrostatic force. These findings correlate with the results of molecular dynamics simulations [82], where cholesterol was shown to order individual lipids adjacent to cholesterol molecules, but abolished the long–range cooperativity between lipids, characteristic for the gel phase with true latticelike spatial order, and altered the lipid electrostatic potential [83]. In the presence of cholesterol [84] it was shown that the membrane electrostatic potential has a much larger variance depending on the distance along the bilayer normal, compared with that for a pure DPPC bilayer.

21.4
Interaction Forces Measured on Lung Epithelial Cells in Buffer

Elevated levels of ultrafine particles in air pollution are associated with increased morbidity and mortality [85]. Unlike larger particles, ultrafine particles reach the peripheral lung and are able to cross the various barriers of the lung, including

the lipid–protein layer of pulmonary surfactant at the air–alveolar interface and the cell membranes of the epithelial and endothelial cells underneath and reach the bloodstream [86–89]. The toxicity of inhaled nanoparticles entering the body through the lung is thought to be initially defined by the electrostatic and adhesive interaction of the particles with the wall of the lung, and lung epithelial cells. Because of their substantial uptake, ultrafine particles are also of great interest for delivery of drugs to the peripheral lung and the body. Despite the importance of the early penetration steps in the biological effects of inhaled particles, the nature of the interactions with the various barriers of the lung remain poorly understood. A detailed study, therefore, promises substantial progress in the understanding of the health threat posed by fine and ultrafine air pollutants and the effectiveness of drug delivery by aerosols. The adhesive interaction includes electrostatic, van der Waals, steric, and hydrophobic forces as well as the line tension between particle, cell, and aqueous medium and depends on the elastic and plastic properties of the cell. The free energy due to these interactions will be minimized upon particle wetting by the lining layer. The lower the surface free energy of the particle, the less it will be wetted by the cell. A thermodynamic model using the "wettability criterion" was indeed successful in predicting passive particle uptake by cells [90]. Another thermodynamic analysis combined with a molecular dynamics simulation found negative line tension values for nanometer-sized particles, but positive values for those an order of magnitude larger [91]. The engulfment of particles in the nanometer range by unbalanced capillary forces was first suggested by Shanahan [92].

We demonstrated that the initial thermodynamic aspects and the time course of the uptake of nanoparticles by lung epithelial cells can be studied using AFM [93] in the force measurement mode. We investigated the first steps of the interaction of nanoparticles with lung epithelial cells using the atomic force microscope as a force apparatus. The apex of theatomic force microscope tip can be used as a model of the nanoparticles, thereby enabling the monitoring of the interaction forces between the nanoparticles and the cell over time. The adhesion force and the work of adhesion have been investigated and correlated with the mechanical properties of the cell.

21.4.1
Cell Culture/Force Measurement Setup

Lung epithelial cells, type II, were isolated from male, pathogen-free Sprague-Dawley rats weighing 150–250 g. The cells were cultured at 6×10^8 cells per milliliter in Dulbecco's modified Eagle's medium supplemented with 1% L-glutamine, containing 10% heat-inactivated fetal bovine serum, and 300 μl of a penicillin–gentamycin solution in γ-irradiated culture dishes. The cells were grown on light microscope glass cover slips. The cells were kept in an incubator under 5% CO_2 and at 37 °C until they created a monolayer with approximately 80% of confluence (4–6 days). At this stage, the phenotype of the lung epithelial cells had changed from type II to type I in that the cells were spread out flat on the interface and ceased to produce surfactant.

Lung epithelial cells were first imaged using a light microscope (Zeiss Axiovert 200). For force spectroscopy, a medium-covered cover slip with the cells was mounted in the liquid cell of the atomic force microscope. The setup used allows for

the observation of the sample and the atomic force microscope cantilever across the cover slip from below by an inverted light microscope at the same time as force spectroscopy (or AFM imaging) is performed. The tip of the atomic force microscope was thus placed over a suitable cell and cell location was under light-microscope control (Fig. 21.10a). Figure 21.10b shows a typical force scan where the cantilever deflection was monitored as a function of the sample position.

At first, the probe approached the cell with the lever undeflected (horizontal line of the force trace), indicating no interaction. The tip then made contact with the sample and became deformed. Forces of interaction between the probe and the cell were then measured in medium at 35 °C, by approach of the tip to the cell interface until a preset load was reached (trace of force curve). The force was acquired as a function of the tip–sample separation h. After the tip has come into contact with the cell, h becomes the penetration depth for the tip into the cell. Separate force curves were acquired for a preset load of 100, 200, and 300 pN. The tip was now kept in contact with the cell for a predetermined time (delay time), while the preset load was kept constant under feedback control (i. e., when the load decreased, the tip was moved forward). We varied the delay time from 0 to 1800 s. Thereafter, the tip was retracted and the adhesion observed. Cantilevers (Micromash), with a spring constant of 57 mN/m, and pyramidal silicon nitride tips were used (tip height 2.9 nm, tip radius less than 20 nm (typical 10 nm), tip angle (face to face) $25-45°$ (top to around 300 nm down). Cells were kept in the medium at all times. The spring constant for each cantilever was measured before and after the experiment using the procedures implemented by the manufacturer of the atomic force microscope

A
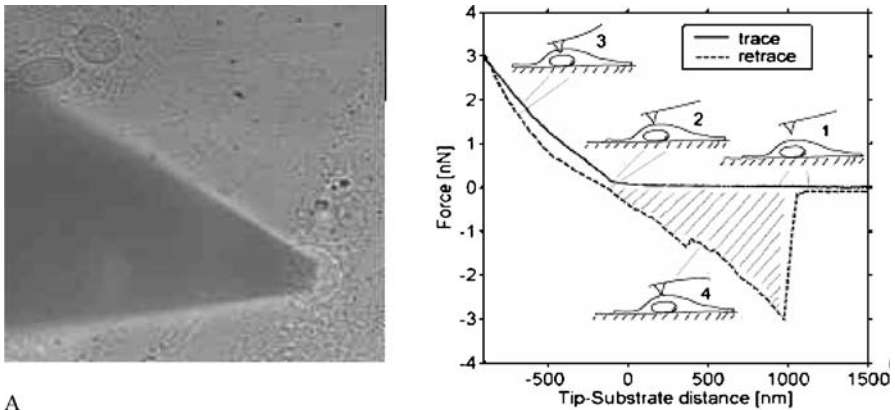
Fig. 21.10. Optical microscopy image of epithelial type II cells and atomic force microscope cantilever. For force spectroscopy, an atomic force microscope tip was placed over the central region of a cell. Trace and retrace force curves were measured on a cell. Force versus tip–sample separation is shown in **b**. The approach part (trace) reveals how the cell deforms upon contact by the tip. The retrace or withdraw part of the curve reveals a large adhesion peak which is often split in multiple peaks. The sketches explain the physical situation for each part of the curve. The *hatched area* denotes the work of adhesion (adhesion energy) between the tip and the cell. The atomic force microscope tip was allowed to stay in contact for various times (delay time) in position $3

(thermal noise method). The sensitivity and the spring constant were found to be not different before and after the experiment.

Forces of interaction between the probe and the cell were then measured in the medium at 35 °C.

21.4.2
Mechanical Properties

The approach part of the force curve was used to determine the penetration depth of the tip into the cell as well as the mechanical properties of the sample. Reviews on this topic are given in [94, 95].The measurement of the penetration depth will depend on the accurate determination of the contact point between the tip and the cell. A cantilever spring constant lower than or similar to that of the cell is preferable. In this case, we can assume that the contact point corresponds in the trace force curve to the first upward deflection. After the tip has come into the contact with the cell, D becomes the penetration depth h of the tip into the cell. To evaluate the mechanical properties of the sample from the approach force profile, the Sneddon model was employed [26, 96]. Note that the use of macroscopic physical law should be reserved for homogeneous bulk materials. Young's modulus should be viewed as an effective parameter to analyze the trend of the in-plane organization of supramolecular structures. The effective parameter can differ from one experiment to another. A more sophisticated approach was to model the mechanical response of the cell membrane explicitly taking into account the mechanics of the cell membrane and that of the underlying cytoskeleton [97]. As the penetration depth h can reach 1 μm, the tip shape must be considered as a function of h. The effective Young's modulus, E', was estimated point by point for h considering the three regions determined by the geometry of the tip [98].

For h between 0 and 10 nm, the AFM probe was considered as a semisphere with a radius R of 10 nm :

$$E_{\text{sphere}} = \frac{3}{4\sqrt{R}} \frac{F}{h^{3/2}} \ . \tag{21.6}$$

For further penetration, the tip profile was viewed as a cone whose half angle varies linearly from $\alpha_1 = 25°$ at $h = 10$ nm to $\alpha_2 = 45°$ when h reaches 300 nm:

$$E_{\text{cone}} = \frac{\sqrt{2}}{\tan \alpha} \frac{F}{h^2} \ . \tag{21.7}$$

For an indentation deeper than 300 nm, α is considered constant to α_2.

Figure 21.11 shows the change in the Young's modulus when increasing the penetration depth h. At first, the tip experienced a layer of increasing stiffness to a penetration depth of about 100 nm, at which point the resistance of the cell to penetration reached a maximum. Thereafter the cell became more compliant again. The stiff layer may represent the outer layer of the cytoskeleton anchored to the cell membrane. The Young's modulus of the membrane can be thought of as the surface tension of the membrane (0.5 N/m) divided by the thickness of the membrane (around 10 nm), i. e., a pressure of around 50 MPa. The lipid head is responsible

Fig. 21.11. When analyzing the approach curve, one can determine the Young's modulus of the sample surface. Young's modulus, which gives a measure of cell elasticity in our case, was found to depend on indentation depth, showing two distinctive parts of the plot: when the peripheral part of the cell was penetrated, up to about 100 nm into the cell, the cell became increasingly stiffer. The stiffness then dropped sharply upon further penetration until it leveled out after penetration to about 200 nm deep
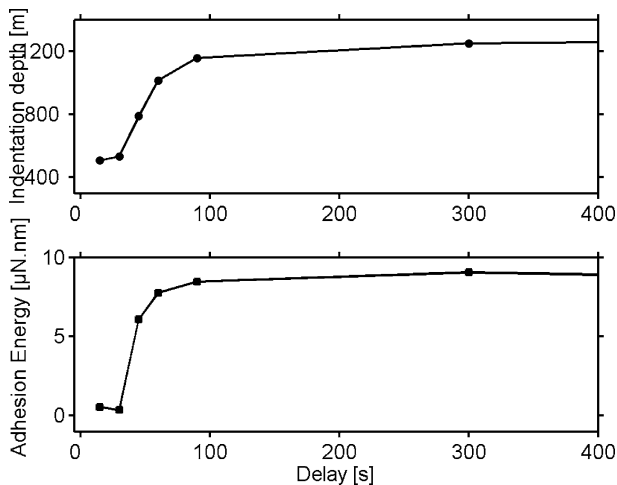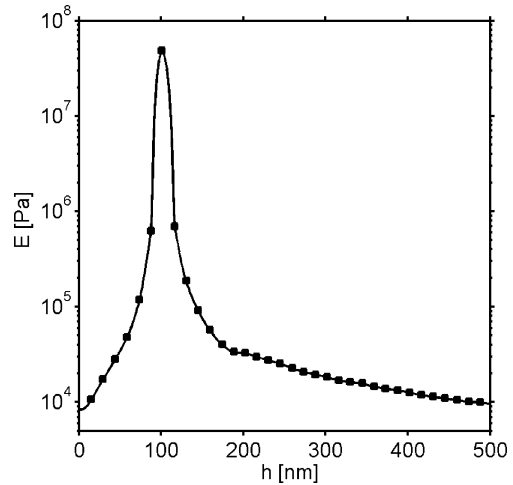
Fig. 21.12. *Top*: Indentation depth as a function of time. The load was kept constant at 200 pN. At time zero, the indentation was about 500 nm. Over time, the tip first penetrated rapidly and then slowly from 500 to 1300 nm. This is evidence of a time-dependent response of the cell to the tip. *Bottom*: Adhesion energy as a function of time. The tip was kept in contact with the cell at a constant load of 200 pN. The longer the tip stays in contact with the cell, the larger the adhesion that is observed. Statistical analysis shows that considerable changes occur during the first 100 s, after which the mean value of the adhesion energy no longer changes

for crystalline elasticity, i.e., the change in the head-to-head distance can change (high elasticity but low rupture). The lipid chain behaves with rubber elasticity (low elasticity), which is related to the change of entropy (increase of order upon pressure). It results in the properties that the cell membranes can be easily deformed in the plane but do not resist the expansion (increase between the headgroup cannot vary more than 2%).

Further measurements of the Young's modulus of cells have been performed with human platelet cells ($E = 1 - 50$ kPa) [99], cardiac cells ($E = 100$ kPa), skeletal muscle cells ($E = 25$ kPa), and endothelial cells ($1 - 7$ kPa) [100].

The analysis of the forced indentation of the epithelial cells by the tip reveals the fate of a nanoparticle coming into contact with the lung's epithelium and then being actively loaded onto a cell. This situation will indeed occur in the lung. The lung's epithelium towards the air is covered by a thin aqueous layer and a molecular film of pulmonary surfactant at the air–water interface. Transmission electron microscopy of lung thin sections as well as scanning electron microscopy of the lung have indeed shown that particles trapped between the surfactant layer and the epithelial cells strongly deform the cells [101, 102].

The penetration depth was also investigated as a function of the contact time between the tip and the cell at a given load. Figure 21.12 shows that the tip first penetrated the cell down to 500 nm in less than 100 s. Equilibrium was reached for approximately 1-μm depth (around half of the cell thickness). We assume that the tip is either actively taken up or the cell rearranges its plasma membrane and the cytoskeleton elements to accommodate the tip.

21.4.2.1
Adhesion Work

After the initial indentation, the tip was kept loaded onto the cell with 1 nN for preset times ranging from 0 to 900 s under feedback control. Thereafter, the tip was retracted and the tip adhesion was acquired.

The retrace curve was used to calculate the adhesion energy Γ between the tip and the cell:

$$\Gamma = \sum_{h_1}^{h_2} F_{\text{retrace}}(h_i)(h_{i+1} - h_i) . \tag{21.8}$$

$F_{\text{retrace}}(h_i)$ is the adhesion force at h_i. The point of the initial contact between the tip and the cell surface, h_1, was determined from the approach part of the force curve; h_2 corresponds to the last jump out of contact.

Upon the penetration into the cell, the adhesion energy also increases. This indicates that the tip becomes engulfed by the membrane and the area of interaction increases (Fig. 21.12). Our results suggest that the process of particle uptake by lung epithelial cells occurs over approximately 100 s. This appears to be the time necessary for the nanoparticle to increase its surface area in contact with the cell and, hence, its adhesive interaction. Other authors have also shown [103] that the increase in adhesion between a polystyrene sphere to mica with increasing load or contact time is due to the plastic deformation. Load dependence and contact time dependence also indicate plastic and viscoelastic deformation [104]. A linear dependence of adhesion force on the reduced radius $R_{\text{eff}} = R_1 R_2/(R_1 + R_2)$, where R_1 and R_2 are the radii of the two particles, was found by Heim et al. [105].

Particles of 50–100 nm in diameter are not phagocytosed [106, 107]. They enter cells in the absence of clathrin and caveolin, associated with active uptake. Even

Fig. 21.13. Correlation between the indentation depth (Fig. 21.12, top) and the adhesion energy (Fig. 21.12, bottom) for all the measurements (around 100 points). The deeper the indentation, the higher is the adhesion energy
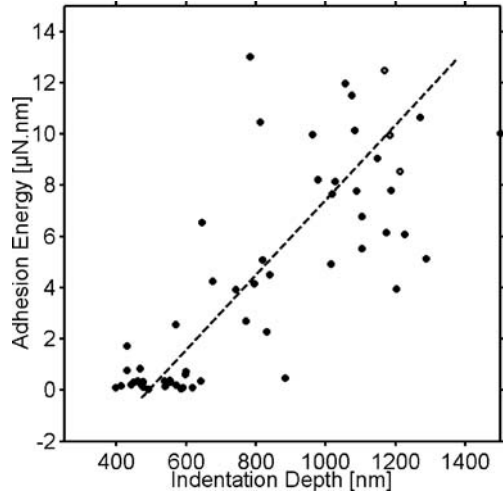
when an actin-based mechanism has been ruled out [107], nanoparticles inside a cell are not surrounded by membrane and, hence, are not taken up through vesicle formation.

The AFM investigation suggests the adhesive interaction in particle uptake can now be measured by our approach and used as a significant parameter test. Particles with different surface properties and different geometries can be mimicked by modified atomic force microscope tips. The adhesive interaction of a particle with the plasma membrane in the lung depends also on the particle history. Airborne particles, after crossing a surfactant layer at the air–water interface of a cell culture dish, have been shown to be more readily taken up than particles added to the media [108]. They may have become coated with a film of pulmonary surfactant and, as a consequence, have penetrated the epithelial cells differently. Whether this is related to a change in adhesive interaction can be tested by coating atomic force microscope tips with surfactant.

21.5
Conclusions

Measurements of forces with the atomic force microscope can determine the local changes in the mechanical and electrical properties induced by the absorption of proteins within lipid monolayers or bilayers. Such studies have offered new perspectives in the identification and characterization of the pulmonary surfactant films in air, model membranes in liquid media, as well as cell membranes in media.

In air, the adhesion forces of particles are known to be 10 times higher than in aqueous media. For a given applied load, the differences in the magnitude of the force do not depend on the contact area, which is similar in air or in a liquid. In fact, the van der Waals forces are screened under a liquid, thereby reducing the total adhesion forces. However, the adhesion forces can be modulated by varying the

contact area between the particle and the layer. We have shown that the temperature or the anesthetic incorporation can largely modify the fluidity of the membrane.

Using the AFM probe as a nanoparticle model is an idea to evaluate the ability of the particle to interact with the cell. Although many kinds of force curve cannot yet be interpreted, for instance, the role of the hydrophobic attraction between tails, our work is a starting point to understand how the particle can penetrate through the lipid layer. For example, the nonnegligible role of the electrical forces in air has been proved and the electrical potential of the layer is of importance in the adsorption process involving the electrical barrier.

The mechanical properties of the cell, and in general the plastic deformation, have been investigated. The role of the membrane as a mechanical barrier is clearly observed by measuring the Young's modulus as a function of the penetration depth. Those properties depend on many parameters: the particle speed, the particle size, the applied load. Also, the duration of the contact is crucial in the incorporation ability of the particles. The complexity of the phenomenon cannot of course be satisfactorily and fully described, but some empirical trend can be locally and statistically defined.

References

1. Cullis PR, Dekruijf B (1979) Biochim Biophys Acta 559:399–420
2. Seelig J, Seelig A (1980) Q Rev Biophys 13:19–61
3. Brown DA, London E (1998) J Membr Biol 164:103–114
4. Nagle JF, Tristram-Nagle S (2000) Biochim Biophys Acta Rev Biomembr 1469:159–195
5. Bloom M, Evans E, Mouritsen OG (1991) Q Rev Biophys 24:293–397
6. Brown DA, London E (2000) J Biol Chem 275:17221–17224
7. Brown DA, London E (1998) Annu Rev Cell Devel Biol 14:111–136
8. Vangolde LMG, Batenburg JJ, Robertson B (1988) Physiol Rev 68:374–455
9. Lewis JF, Jobe AH (1993) Am Rev Respir Dis 147:218–233
10. Possmayer F (1988) Am Rev Respir Dis 138:990–998
11. Vedhuizen R, Nag K, Orgeig S, Possmayer F (1998) Biochim Biophys Acta Mol Basis Dis 140:890–108
12. Rooney SA, Young SL, Mendelson CR (1994) FASEB J 8:957–967
13. Tamm LK, McConnell HM (1985) Biophys J 47:105–113
14. Tien HT, Ottova AL (1998) Electrochim Acta 43:3587–3610
15. Heyse S, Ernst OP, Dienes Z (1998) Biochemistry 37:507–522
16. Muller RH, Mader K, Gohla S (2000) Eur J Pharma Biopharma 50:161–177
17. Leonenko ZV, Carnini A, Cramb DT (2000) Biochim Biophys Acta 1509:134–140
18. Zasadzinski J, Helm CA, Longo ML, Weisenhorn AL, Gould SAC, Hansma PK (1991) Biophys J 59:755–760
19. Hui SW (1995) Mol Membr Biol 12:45–50
20. Singh S, Keller DJ (1991) Biophys J 60:1401–1410
21. Beckmann M, Nollert P, Kolb HA (1998) J Membr Biol 161:227–233

22. Han W, Lindsay SM, Jing T (1996) Appl Phys Lett 69:4111–4113
23. Han W, Lindsay SM (1998) Appl Phys Lett 72:1656–1658
24. Fasolka MJ, Mayes AM (2001) Annu Rev Mater Res 31:323–355
25. Lee GU, Kidwell DA, Colton RJ (1994) Langmuir 10:354–357
26. Cappella B, Dietler G (1999) Surf Sci Rep 34:1–104
27. Senden TJ, Drummond CJ, Ke'kicheff P (1994) Langmuir 10:358–362
28. Cleveland JP, Schäffer TE, Hansma PK (1995) Phys Rev B 52:8692–8695
29. Israelachvili J (2005) Q Rev Biophys 38:331–337
30. Livadaru L, Kovalenko A (2006) Nano Lett 6:78
31. Biggs S (1995) Langmuir 11:156–162
32. Dufrene YF, Boland T, Schneider JW, Barger WR, Lee GU (1998) Faraday Discuss 111:79
33. Finot E, Lesniewska E, Mutin J-C, Goudonnet J-P (1999) J Chem Phys 111:6590–6598
34. Finot E, Lesniewska E, Mutin J-C, Goudonnet J-P (2000) Langmuir 16:4237–4244
35. Finot E, Lesniewska E, Mutin J-C, Goudonnet J-P (2000) Appl Surf Science 161:316–322
36. Butt HJ, Cappella B, Kappl M (2005) Surf Sci Rep 59:1–152
37. Finot E, S Roualdes, Kirchner M, Rouessac V, Berjoan R, Durand J, Goudonnet J-P, Cot L (2002) Appl Surf Sci 187:326–338
38. Mollica V, Relini A, Rolandi R, Bolognesi M, Gliozzi A (2000) Eur Phys J E 3:315
39. Van EW der Vegte, Hadziioannou G (1997) Langmuir 13:4357–4368
40. Dimitriadis EK, Horkay F, Maresca J, Kachar B, Chadwick RS (2002) Biophys J 82:2798–2810
41. Legay G, Finot E, Meunier-Prest R, Cherkaoui-Malki M, Latruffe N, Dereux A (2005) Biosens Bioelectron 21:627–636
42. Franz V, Loi S, Muller H, Bamberg E, Butt H-J (2002) Colloids Surf B 23:191–200
43. Butt HJ, Franz V (2002) Phys Rev E 66:1601
44. Loi S, Sun G, Franz V, Butt HJ (2002) Phys Rev E 66:1602
45. Tenchov B, Koynova R, Rapp G (2001) Biophys J 80:1873–1890
46. Meyer HW, Semmler K, Rettig W, Pohle W, Ulrich AS, Grage S, Selle C, Quinn PJ (2000) Chem Phys Lipids 105:149–166
47. Bizzotto D, Nelson A (1998) Langmuir 14:6269–6273
48. Tamm LK (1985) Biol Chem Hoppe-Seyler 366:859–859
49. Kalb E, Frey S, Tamm LK (1992) Biochim Biophys Acta 1103:307–316
50. Nollert P, Kiefer H, Jahnig F (1995) Biophys J 69:1447–1455
51. Exerowa D (2002) Adv Colloid Interface Sci 96:75–100
52. Ebel H, Grabitz P, Heimburg T (2001) J Phys Chem B 105:7353–7360
53. Giocondi MC, Vie V, Lesniewska E, Milhiet PE, Zinke-Allmang M, Le C Grimellec (2001) Langmuir 17:1653–1659
54. Leonenko Z, Cramb D (2002) Nano Lett 2:305–309
55. Leonenko ZV, Merkle DD, Lees-Miller SP (2002) Langmuir 18:4873–4884
56. Tokumasu F, Jin AJ, Dvorak JA (2002) J Electron Microsc 51:1–9
57. Leonenko Z, Cramb D (2004) Can J Chem 82:1–11
58. Leonenko Z, Finot E, Cramb D (2006) Biochim Biophys Acta Biomembr 1758:487–492
59. Leonenko ZV, Carnini A, Cramb DT (2000) Biochim Biophys Acta 1509:131–147
60. Brian AA, McConnell HM (1984) Proc Natl Acad Sci USA 81:6159–6163
61. Leonenko ZV, Finot E, Ma H, Dahms T, Cramb DT (2004) Biophys J 86:3783–3793
62. Shamrakov LG, Leonenko Z, Finot E, Cramb DT (2006) Aust J Chem 59:386–389
63. Biltonen RL, Lichtenberg D (1993) Chem Phys Lipids 64:129–142
64. Yang J, Appleyard J (2000) J of Phys Chem B 104:8097–8100
65. Binnig G, Quate CF, Gerber C (1986) Phys Rev Lett 56:930–933
66. Israelachvili J (1992) Intermolecular and surface forces. Academic, New York
67. Williams JM, Han T, Beebe TP (1996) Langmuir 12:1291–1295

68. Marrink SJ, Berger O, Tieleman P (1998) Biophys J 74:931–943
69. Evans K, Evans MF, Laker MF (1995) Ann Clin Biochem 32:261–280
70. Butt HJ (1991) Biophys J 60:1438–1444
71. Butt HJ, Franz V (2002) Phys Rev E 66:1601
72. Carnini A, Phillips HA, Shamrakov LG, Cramb DT (2004) Can J Chem 82:1139–1149
73. Garcia-Manyes S, Oncins G, Sanz F (2005) Biophys J 89:4261–4274
74. de Gennes PG (1987) Adv Colloid Interface Sci 27:189–209
75. Petrache HI, Dodd SW, Brown MF (2000) Biophys J 79:3172–3192
76. Nagle JF, Tristram-Nagle S (2000) Biochim Biophys Acta Rev Biomembr 1469:159–195
77. Janiak MJ, Small DM, Shipley GG (1979) J Lipid Res 20:183–199
78. Gunasekara L, Schurch S, Schoel WM (2005) Biochimi Biophys Acta Mol Cell Biol Lipids 1737:27–35
79. Leonenko Z, Finot E, Amrein M (2007) Ultramicroscopy 107:948–953
80. Leonenko Z, Rodenstein M, Dohner J, Eng LM, Amrein M (2006) Langmuir 22:10135–10139
81. Leonenko Z, Gill S, Baoukina S, Monticelli L, Doehner J, Gunasekara L, Felderer F, Rodenstein M, Eng LM, Amrein M (2007) Biophys J 93:674–683
82. Chiu SW, Jakobsson E, Scott HL (2001) J Chem Phys 114:5435–5443
83. Smondyrev AM, Berkowitz ML (1999) J Chem Phys 111:9864–9870
84. Smondyrev AM, Berkowitz ML (1999) J Chem Phys 110:3981–3985
85. Atkinson RW, Anderson HR, Strachan DP, Bland JM, Bremner SA, de Leon AP (1999) Eur Respir J 13:257–265
86. Oberdorster G, Sharp Z, Atudorei V, Elder A, Gelein R, Lunts A, Kreyling W, Cox C (2002) J Toxicol Environ Health 65:1531–1543
87. Geiser M, Rothen-Rutishauser B, Kapp N, Schurch S, Kreyling W, Schulz H, Semmler M, Hof VI, Heyder J, Gehr P (2005) Environ Health Perspect 113:1555–1560
88. Nemmar A, Hoet PHM, Vanquickenborne B, Dinsdale D, Thomeer M, Hoylaerts MF, Vanbilloen H, Mortelmans L, Nemery B (2002) Circulation 105:411–414
89. Takenaka S, Karg E, Roth C, Schulz H, Ziesenis A, Heinzmann U, Schramel P, Heyder J (2001) Environ Health Perspect 109:547–551
90. Chen H, Langer R, Edwards DA (1997) J Colloid Interface Sci 190:118–133
91. Bresme F, Quirke N (1999) J Chem Phys 110:3536–3547
92. Shanahan MER (1990) J Phys D Appl Phys 23:321–327
93. Le C Grimellec, Lesniewska E, Gioconda MC et al (1998) Biophys J 75:695–703
94. Costa KD (2003) Dis Markers 19:139–154
95. Radmacher M (2002) Methods Cell Biol 68:67–90
96. Sneddon JN (1965) Int J Eng Sci 3:47
97. Mc MElfresh, Baesu E, Balhorn R, Belak J, Allen MJ, Rudd RE (2002) Proc Natl Acad Sci USA 99:6493–6497
98. Stark RW, Drobek T, Weth M, Frickef J, Heckel WM (1998) Ultramicroscopy 75:161
99. Radmacher M, Fritz M, Kacher CM, Cleveland JP, Hansma PK (1996) Biophys J 70:556–567
100. Mathur AB, Collinsworth AM, Reichert WM, Kraus WE, Truskey GA (2001) J Biomech 34:1545–1553
101. Bachofen H, Schurch S, Possmayer F (1994) J Appl Physiol 76:1983–1992
102. Gehr P, Geiser M, Im V Hof, Schurch S, Waber U, Baumann M (1993) Microsc Res Tech 26:423–436
103. Biggs S, Spinks G (1998) J Adhes Sci Technol 12:461–478
104. Reitsma M, Craig VSJ, Biggs S (2000) J Adhes 74:125–142
105. Heim LO, Blum J, Preuss M, Butt H-J (1999) Phys Rev Lett 83:3328–3331

106. Geiser M, Rothen-Rutishauser B, Kapp N, Schurch S, Kreyling W, Schulz H, Semmler M, Hof VI, Heyder J, Gehr P (2005) Environ Health Perspect 113:1555–1560
107. Rothen-Rutishauser BM, Schurch S, Haenni B, Kapp N, Gehr P (2006) Environ Sci Technol 40:4353–4359
108. Blank F, Rothen-Rutishauser BM, Schurch S, Gehr P (2006) J Aerosol Med 19 (in press)